Third Annual Progress Report

Pulsed Thermal Tomography Nondestructive Examination of Additively Manufactured Reactor Materials and Components

Nuclear Science and Engineering Division

Third Annual Progress Report

Pulsed Thermal Tomography Nondestructive Examination of Additively Manufactured Reactor Materials and Components

prepared by
Alexander Heifetz[1], Victoria Ankel[1,2], Xin Zhang[1,3], Jafar Saniie[3], , Sasan Bakhtiari[1]

[1]Nuclear Science Engineering Division, Argonne National Laboratory
[2]Department of Physics, University of Chicago, Chicago, IL
[3]Department of Electrical and Computer Engineering, Illinois Institute of Technology, Chicago, IL

December 29, 2021

Table of Contents

List of Figures

Abstract

Additive manufacturing (AM) of high-strength corrosion resistance alloys for nuclear energy applications, such as stainless steel and Inconel, is currently based on laser powder bed fusion (LPBF) process. Some of the challenges with using LPBF method for nuclear manufacturing include the possibility of introducing pores into metallic structures. Probability of crack initiation at the pore depends on size, shape, and orientation of the defect. Pulsed Infrared Thermography Imaging (PIT) provides a capability for non-destructive evaluation (NDE) of sub-surface defects in arbitrary size structures. The PIT method is based on recording material surface temperature transients with infrared (IR) camera following thermal pulse delivered on material surface with flash light. The PIT method has advantages for NDE of actual AM structures because the method involves one-sided non-contact measurements and fast processing of large sample areas captured in one image. Following initial qualification of an AM component for deployment in a nuclear reactor, a PIT system can also be used for in-service nondestructive evaluation (NDE) applications. In this report, we describe recent progress in enhancing PIT capabilities in detecting microscopic subsurface defects in metals, and classifying shapes and orientation of pores in thermal images. For detection of microscopic defects in PIT imaging data, we have developed Spatial Temporal Denoised Thermal Source Separation (STDTSS) unsupervised machine learning (ML) image processing algorithm. We show that flat bottom hole (FBH) defects as small as 200µm in SS316 and IN718 specimens, can be detected with STDTSS algorithm. To the best of our knowledge, these are the smallest detected defects which are reported in literature. For classification of defects shapes, we have previously developed thermal tomography (TT) algorithm to obtain depth reconstructions of material defects from data cube of sequentially recorded surface temperatures. However, interpretation of TT images is non-trivial because of blurring with increasing depth. To address this challenge, we have developed a deep learning convolutional neural network (CNN) to classify size and orientation subsurface defects in simulated TT images.

1. Introduction

Additive manufacturing (AM) of metals is an emerging method for cost-efficient production of low volume custom structures from high-strength corrosion-resistant alloys for nuclear energy applications [1]. Metals of interest for passive structures in light water reactors, as well as high-temperature liquid metal and molten salt-cooled advanced reactors include, include stainless steel 316L (SS316L) and Inconel 718 (IN718). Because of high melting temperature of these alloys, AM of SS316L and IN718 is currently based on laser powder-bed fusion (LPBF) process [2]. Due to the intrinsic features of LPBF process, pores can appear in 3D printed metallic structures [3]. Because of stringent safety requirements, each AM metallic structure needs to be qualified through nondestructive examination before deployment in a nuclear reactor [4].

Typical porosity defects observed in LPBF manufacturing consist of microscopic spheroidal-shape keyhole pores caused by excessive laser power, irregular-shape lack of fusion (LOF) pores caused by insufficient laser power, and spherical gas pores caused by trapped of gas in solidifying melt pool. Typical sizes of keyhole and LOF pores in tens to hundreds of microns, while gas pores sizes are on the order of a few microns. Prior studies indicate that larger size pores located closer to surface, and oriented with major axis perpendicular to surface plane, are more likely to cause fatigue crack initiation [5,6].

In principle, high-resolution imaging with X-ray or neutron computed tomography (CT) can be used for high-resolution imaging pores in metals. However, applications of high-resolution X-ray CT are typically limited to small coupons with body-of-revolution shapes (cylinders and spheres). Neutron CT has a larger penetration depth, but has a potential side effect of activating the metal. Ultrasonic testing is scalable with structure size, but face challenges because the rough surfaces, characteristic of AM structures, affect the probe coupling. For high-resolution ultrasonic tomography, imaging of large structures is time-consuming because of point-by-point raster scanning of specimens. Pulsed Infrared Thermography (PIT) offers several potential advantages because measurements are one-sided, non-contact, and scalable to arbitrary size structures [7-14]. The PIT method consists of recording material surface temperature transients with an infrared (IR) camera, following deposition of a thermal pulse.

The objective of work discussed in this report is to develop advanced image processing capabilities for detection of subsurface microscopic pores in AM structures with PIT. In prior studies, we have demonstrated the capability of PIT in detection of calibrated defects in SS316L and IN718. The calibrated defects consisted of (1) hemispherical regions containing un-sintered powder, which were imprinted into metallic specimens during LPBF manufacturing, (2) flat bottom hole (FBH) indentations in metallic specimens. In prior work, the smallest detected defect, either an imprinted hemisphere or an FBH was a 1mm-diameter feature [15]. For microscopic defects, thermal signature intensity is approaching the detection sensitivity level of IR camera. In a recent work, we have developed Spatial Temporal Denoised Thermal Source Separation (STDTSS) ML algorithm for processing PIT images [11,16]. The STDTSS involves spatial and temporal denoising using Gaussian filtering and Savitzky–Golay filtering, followed by the matrix decomposition using Principal Component Analysis (PCA), and Independent Component Analysis

4

(ICA), to automatically detect flaws in images. In the work described in this report, we use STDTSS algorithm for processing of PIT images of metallic specimens with microscopic FBH defects created with EDM (electron discharge machining) drill. The subsurface defects ranged from 200µm to 500µm in diameter, with depths below the surface ranging from 100µm to 500µm. We show that all FBH defects are detectable in SS316 and IN718 specimens at depths smaller than 400µm.

In another approach described in this report, we describe development of ML-based classification of shape and orientation of material defects from thermal tomography (TT) reconstructions [14,17]. TT algorithm discussed in our prior work obtains depth reconstructions of spatial effusivity from the data cube of sequentially recorded surface temperatures. However, interpretation of TT images is non-trivial because of blurring of images with increasing depth. In this report, we describe development of a deep learning convolutional neural network (CNN) to classify size and orientation subsurface defects in simulated thermal tomography (TT) images [14,17]. CNN is trained on a database of TT images created for a set of simulated metallic structures with elliptical subsurface voids. Test of CNN performance demonstrate the ability to classify radii and angular orientation of subsurface defects in TT images. In addition, we show that CNN trained on elliptical defects is capable of classifying irregular-shaped defects obtained from scanning electron microscopy (SEM) of stainless steel sections printed with LPBF.

2. Pulsed Infrared Thermal Imaging

In the experimental PTT system, data is acquired with a laboratory setup consisting of a megapixel fast frame infrared (IR) camera and flash lamp is shown in schematic depiction in Figure 1. A pulse trigger sends a signal to capacitor to discharge in a circuit containing white light flash lamp. The flash lamp source delivers a pulse of thermal energy to material surface. Heat transfer takes place from the heated surface to the interior of the sample, resulting in a continuous decrease of the surface temperature. For better heat absorption, and to remove the effect of different surface emissivity, all materials in this study were spray-painted with washable graphite paint. As heat deposited with flash lamp the surface starts diffusing into the material bulk, presence of low-density internal material inclusions is revealed through appearance of local temperature "hot spots" on the surface. This effect occurs because low density defects have lower thermal diffusivity compared with solid material. The defects act as thermal resistances and slow down thermal diffusion, which causes temperature difference on the material surface between regions of defects and non-defects. A megapixel fast frame infrared (IR) camera records blackbody radiation to obtain time-resolved images of surface temperature distribution T(x,y,t). The acquired thermal-imaging data cube therefore consist of a series of 2D images of the sample's surface temperature at consecutive time instants.

The laboratory system for data acquisition uses a FLIR x8501sc with Indium Antimonide (InSb) detector camera, which has integration time of 270ns, NETD sensitivity of <30mK, and frame rate of at 180Hz at full frame imaging. The flash lamp source (Balcar ASYM 6400 in the experiment) delivers a pulse of 6400J/2ms thermal energy to material surface. The flash lamp is typically positioned at 30cm to 50cm distance to the specimen under investigation. The exact distance and angle of illumination of the flash lamp are determined experimentally for each specimen. This is decided by positioning the IR camera at the focal length of the lens, and placing the flash lamp such that the IR field of view is not blocked, nor does IR camera block the flash.
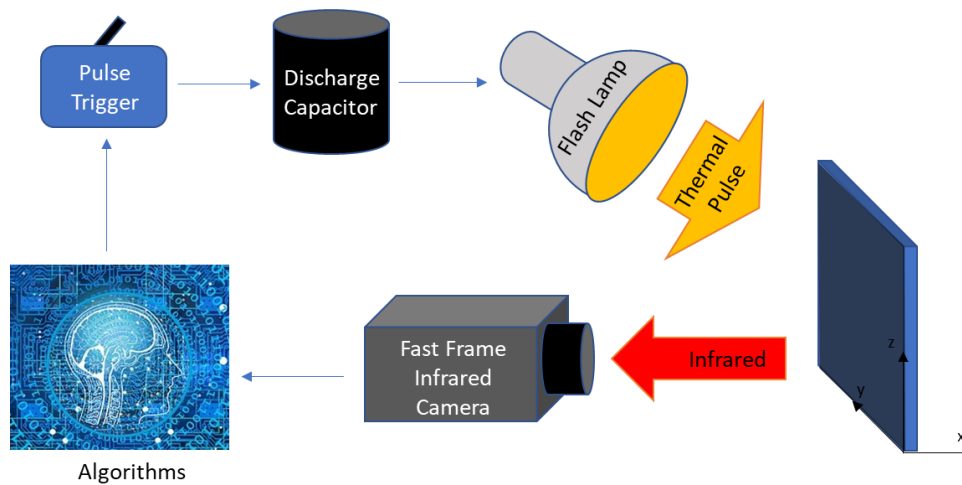
Figure 1 – Schematic drawing of pulsed infrared thermography (PIT) data acquisition setup

Temporal profile of temperature transient following thermal pulse deposition at one location on the plate recorded with a calibrated IR camera is shown in Figure 2. For this particular location on the plate, temperature rises by approximately 50°C. Distribution of temperature on the plate surface can be non-uniform across the plate because flash lamp light is incident at an angle, and because drying paint can aggregate into localized clumps with spatially varying heat absorption characteristics.
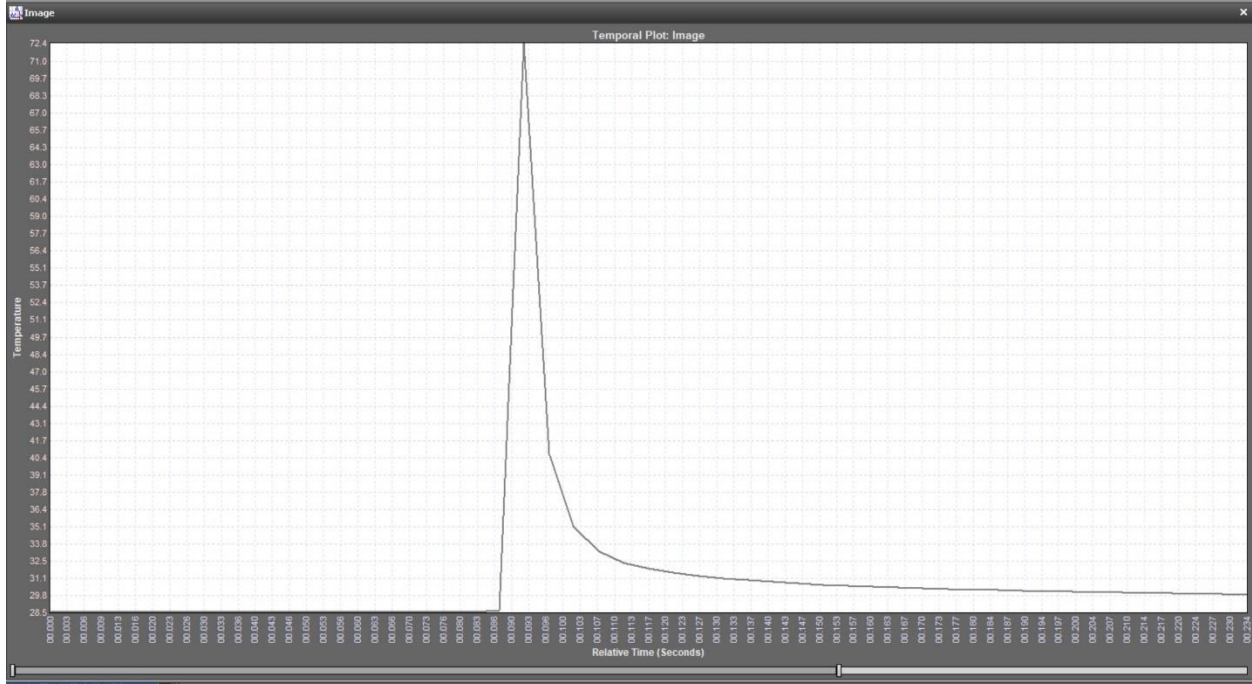
Figure 2 – Temperature transients on plate surface measured with calibrated IR camera at one pixel location

While there have been proposed a number of PIT data analysis approaches based on physics models [18,19] or machine learning [20], these methods have difficulty with detecting weak features in thermography data, which correspond to microscopic material defects. For such thermal signals, signal to noise ratio SNR < 1, with signal amplitude approaching noise equivalent temperature difference (NETD) detectability threshold.

A thermographic signal reconstruction (TSR) method was proposed, which involves curve fitting for temperature transient signals with a fifth to eighth-degree polynomial on a log-log scale [21]. Thermographic sequences fitting based on genetic and differential evolution algorithms were proposed, which improved compression performance by using few fitting coefficients to replace temperature signals. However, this iterative algorithm required a large amount of computation and a long processing time, with limited spatial resolution.

An approach based on the virtual wave concept was developed to estimate specimen thickness from pulsed thermographic data [22,23]. The virtual wave method uses a local transformation kernel to convert "thermal waves" (observed thermographic data) into virtual acoustic waves. Virtual acoustic waves were analyzed with ultrasound reconstruction algorithms, such as the frequency

7

domain synthetic aperture focusing technique, to eliminate the virtual time dimension. However, the thermal to ultrasonic conversion process increased algorithm runtime and potentially led to the loss of information in thermographic images. This reduced the effectiveness of the virtual wave method for applications to the detection of thermal signals with SNR < 1.

A pulse-compression method was developed to detect defects with step heating thermography using halogen lamps [24]. Material defects were detected by convolving the acquired thermograms with a matched filter to estimate true impulse response. This reduced the noise leading to an increased SNR. As an extension of pulse-compression method, a barker-coded thermal wave imaging was proposed to evaluate defects in steel material [25]. A shorter Barker-code (7-bit) was used to process thermograms in the pulse-compression algorithm. The drawback of these methods was that fidelity of the impulse response reconstruction was affected by numerical noise. In addition, experimental measurement of background was required, which increased the complexity of method implementation

A data-processing algorithm for stepped thermography was developed to detect subsurface defects of carbon fiber reinforced polymer (CFRP) using fitting parameters based on Newton's law of cooling [26]. Fitting transient temperature data was accomplished using Gauss-Newton algorithm, and storing the estimated polynomial coefficients for each temperature signal. However, when using the reconstructed temperature matrix, not all material defects were detectable in thermography images due to the loss of information in reconstruction.

3. Detection of Microscopic Defects in SS316 and IN718 Plates

3.1. Spatial Temporal Denoised Thermal Source Separation (STDTSS) Machine Learning Algorithm

Extraction of features of interest from PIT images can be accomplished with machine learning (ML) and image processing algorithms. In thermography images of microscopic defects, signals from features are approaching NETD limit. Therefore, image processing is required to separate signals due to defects from noises due to uneven heating and camera noises. We have recently developed image processing STDTSS algorithm which compensates for thermal image artifacts to enable detection of flaws [11,16]. The flow chart of STDTSS algorithm is shown in Figure 3. The STDTSS algorithm incorporates a number of image denoising features into the STDTSS algorithm. In particular, we design a Gaussian spatial filter and a 7-point Savitzky–Golay temporal filter as preprocessing steps to remove IR imaging noises in space and time. Next, PCA is used to decompose thermography data into principal features, which are fed into ICA implemented as a two-layer neural network structure. The ICA aims to classify and separate the thermography source signals, which correspond to image regions of defects, non-defects, and noise. Each thermography source signal exhibits different temperature evolution during the transient response recorded with PT system. We reconstruct the Thermal Source Image (TSI) from STDTSS to display image regions of defects to detect flaws.

The flow chart of STDTSS algorithm is shown in Figure 3 [11,16]. According to the flow chart, the observed thermograms X are mixed with different thermography source signals which need to be denoised and separated. The Gaussian low pass filter followed by the Savitzky–Golay filter are used to remove noises from thermograms X in space and time. Next, the denoised thermography data cube X' is decomposed with PCA which is implemented as Singular Value Decomposition (SVD) to obtain principal thermography features U. The principal components U are fed as inputs to the neural learning-based ICA for further decomposition and classification to estimate the thermal source signals of defects S_e, which are TSI of defects. Here W is the separation matrix used to estimate the TSI.
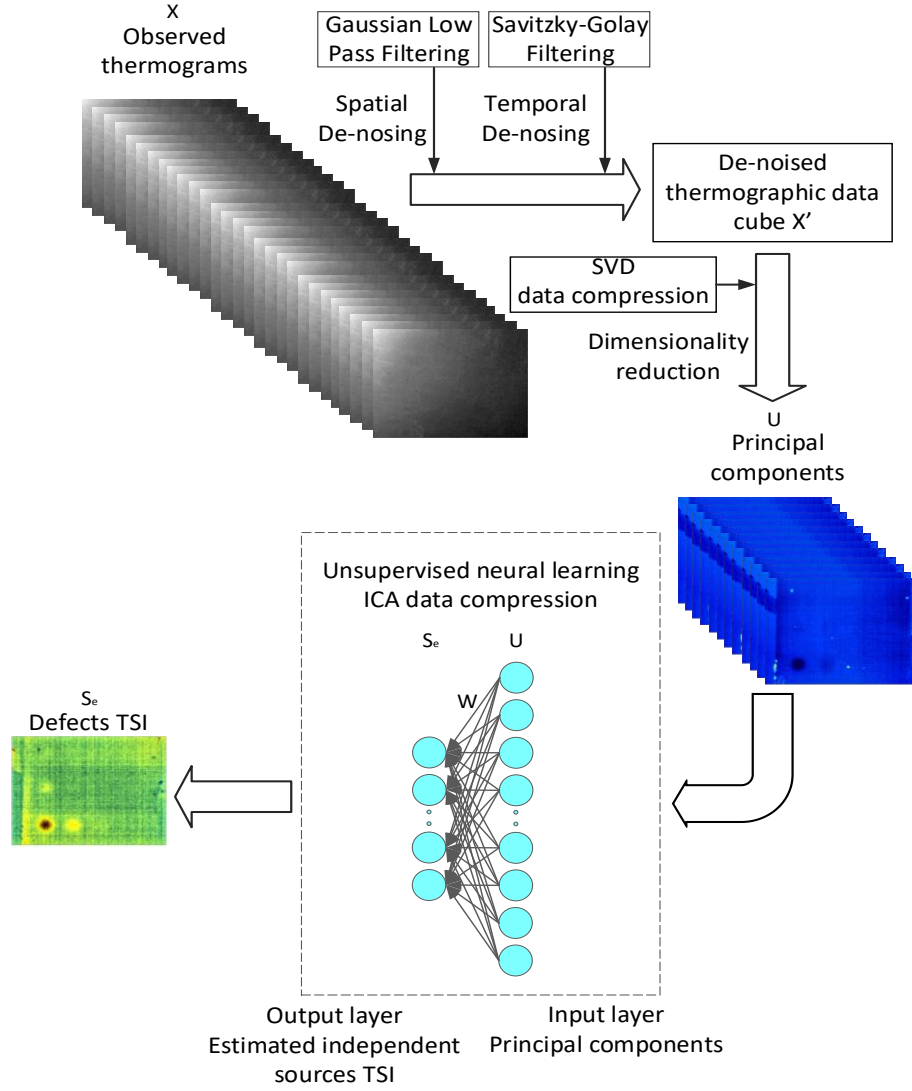
Figure 3 – Flowchart of STDTSS algorithm

We designed a 3x3 Gaussian low pass filter which removes spatial thermography noises. The 2D Gaussian function is defined as

$$G(x, y) = \frac{1}{2\pi\sigma^2} e^{-\frac{x^2+y^2}{2\sigma^2}}$$ (1)

A 3×3 normalized convolution matrix with $\sigma = 0.84$ is produced by the Gaussian function in Equation (1). The matrix H is used to smooth-out the observed thermography images using the convolution process, while preserving the signatures of material defects. The matrix H is given as:

$$H = \begin{bmatrix} 0.06 & 0.13 & 0.06 \\ 0.13 & 0.25 & 0.13 \\ 0.06 & 0.13 & 0.06 \end{bmatrix} \qquad (2)$$

To quantify the denoising performance of the Gaussian spatial filter, we calculate the peak signal-to-noise ratio (PSNR):

$$PSNR = 10\log_{10}\left(\frac{1}{MSE}\right) \qquad (3)$$

Where the MSE stands for the Mean Squared Error between the observed thermography image and Gaussian denoised thermography image. Using Equation (3) for observed thermography images and Gaussian denoised thermography images, we obtain an enhancement of PSNR=40.72dB.

Savitzky-Golay filter is a digital filter using selected convolution coefficients for smoothing the temporal data. In PT, each pixel in thermography image acts as a temporal signal and consists of a set of points (x_j, y_j), where x_j represents the jth time instant and y_j represents the corresponding pixel intensity. These points are noisy in time domain due to thermal imaging noises, but are smoothed by a group of m convolutional coefficients C_i using the following:

$$Y_j = \sum_{i=\frac{1-m}{2}}^{\frac{m-1}{2}} C_i y_{j+i} \qquad (4)$$

Where $\frac{n-1}{2} \leq j \leq n - \frac{1-m}{2}$, and where n is the number of observed thermography images. In this paper, we use the 7-point ($m = 7$) quadratic polynomial convolution coefficients (-2/21, 3/21, 6/21, 7/21, -2/21, 3/21, 6/21) to enhance the precision of data without distorting the thermography signal.

To detect flaws, the denoised thermography data cube X' is decomposed with SVD to extract principal features (U) of defects by removing non-relevant information, such as un-even heating due to flash lamp pulse incident at an angle on the material surface (see Figure 1). Next, the principal features are used as inputs to train the neural learning-based ICA to separate image regions containing signatures of defects from image regions do not contain any material defects. After the separation matrix W is trained using ICA, this matix is applied to detect flaws by separating the mixed thermograhms into TSIs of defects. This neural learning-based ICA consists of one input layer (principal features U), and one output layer (estimated source signal S_e). The input layer has 20 neurons, equal to the number of principal components. The output layer has 8 neurons, equal to the number of independent components. The nonlinearity function "pow3" ($g(u) = u^3$) is used as the activation funtion to optimize training with fast fixed-point algorithm for robust covergence. In addition, the reverse entropy is applied as the objective funciton to measure the non-Gaussian. We train this two-layer neural network with 100 epochs to estimate TSI of defects.

3.2. Development of Microscopic Flat Bottom Hole Defects in SS316 and IN718 Plates

Calibrated FBH defects were introduced into SS316 and IN718 specimens with EDM drill. Prior studies of PIT performance involved calibrated defects introduced as either FBH defects created in metallic specimens with a high-strength drill, or hemispherical inclusions containing un-sintered trapped powder imprinted into metallic specimens during LPBF process. Creating microscopic calibrated defects in high strength metal is a challenge with LPBF process involves sintering SS316 and IN718 metallic powder grains with the average diameters of 20µm and 40µm, respectively. A scanning electron microscope (SEM) micrograph of SS316 TrueForm powder grains is shown in Figure 4(a). The histogram of particle diameter distribution is plotted in Figure 4(b). From the plot, one can observe that particle diameters can be as large as 50µm. Creating imprinted porosity defects with diameters smaller than 300µm with LPBF involves trapping several un-sintered powder grains. Controlling inclusion size at this length-scale is a difficult task because heat diffusion is involved in sintering. In addition, LOF and keyhole inclusion are typically air voids in metal with no trapped powder.

(a)   (b)
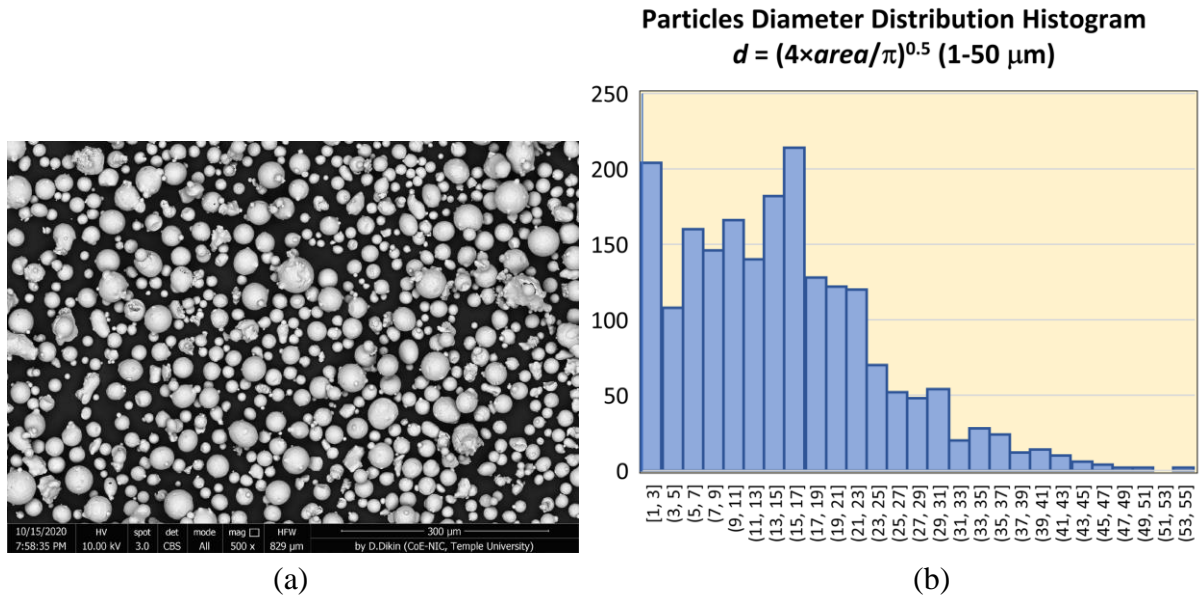
Figure 4 – (a) SEM micrograph of SS316 TrueForm powder grains. (b) Histogram of particle diameter distribution.

Therefore, in developing microscopic calibrated defects, the FBH model of material defect for proof-of-principle studies was selected. FBH defects closely model air voids from heat transfer physics point of view. FBH's can be created to be of precise shapes, diameters and depths relative material surface with an EDM drill. A pattern of microscopic FBH defects introduced into SS316 and IN718 plates with EDM drill is shown in Figure 5(a). There is a matrix of FBH's with diameters ϕ =500µm, 400µm, 300µm, and 200µm. The defects are located at depths d = 100µm, 200µm, 300µm, 400µm, and 500µm below the flat surface. The SS316 and IN718 plates are 3mm

thick. A photograph of the FBH's in SS316 plate is shown in Figure 5(b). A photograph of the flat side of the plate painted with Krylon ultra flat black spray paint is shown in Figure 5(c). Note that a 200μm FBH created with EDM drill in SS316 and IN718 3-mm thick plates corresponds the state-of-the-art limit for most EDM industry.

(a)

(b)

(c)
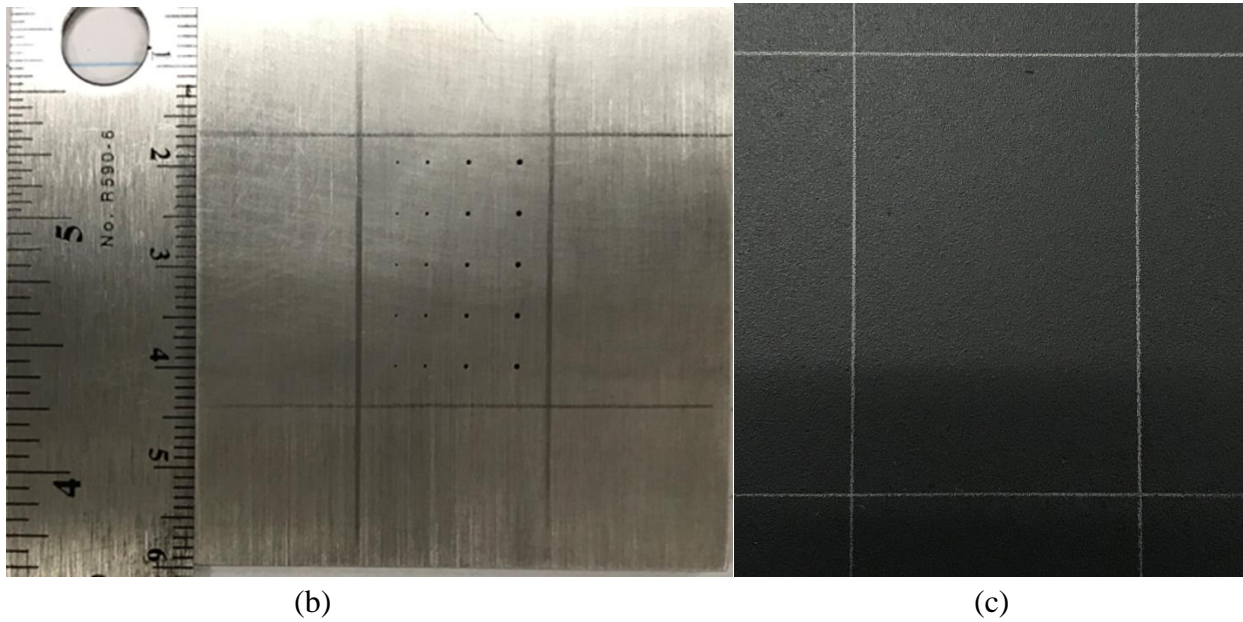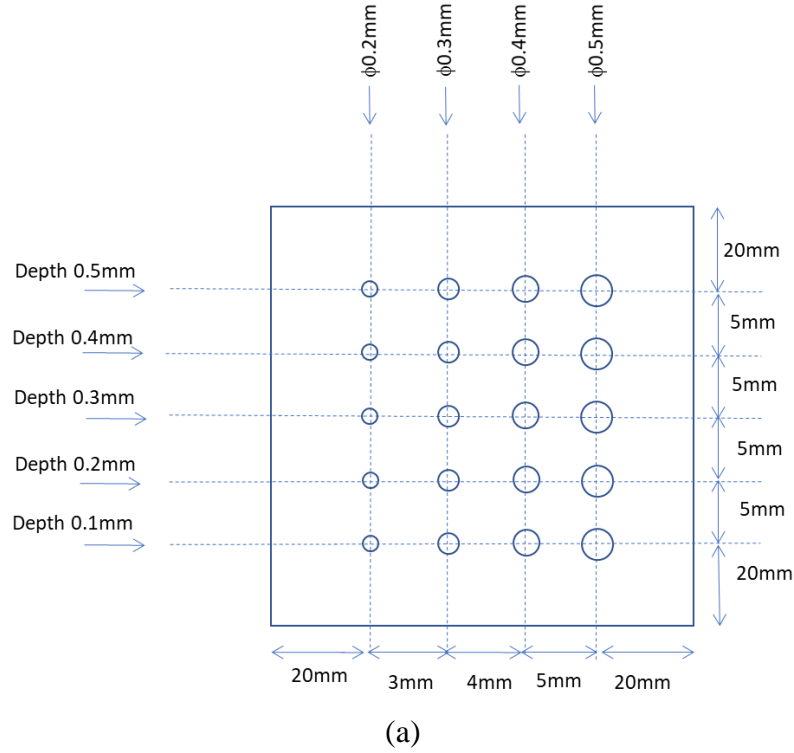
Figure 5 – (a) Photograph of EDM-drilled microscopic FBH's in SS316 plate. (b) Back surface of the plate painted with Krylon ultra flat black spray paint.

3.3. Detection of Microscopic Flat Bottom Hole Defects in SS316 and IN718 Plates with STDTSS Algorithm

In the first experiment, PIT imaging was performed on the SS316 plate. The measurements were made with the painted side plate (See Figure 4(c)) facing the IR camera and the flash lamp. Raw thermograms obtained from the IR camera, such as the one in Figure 6(a), do not show any defects. Image of the plate obtained with STDTSS algorithm is shown in Figure 6(b). All defects at depth at depths up to 300µm, and two larger defects at depth 400µm are clearly visible. To the best of our knowledge, detection of 200µm defect in SS316 is the smallest one reported in literature.

(a) (b)
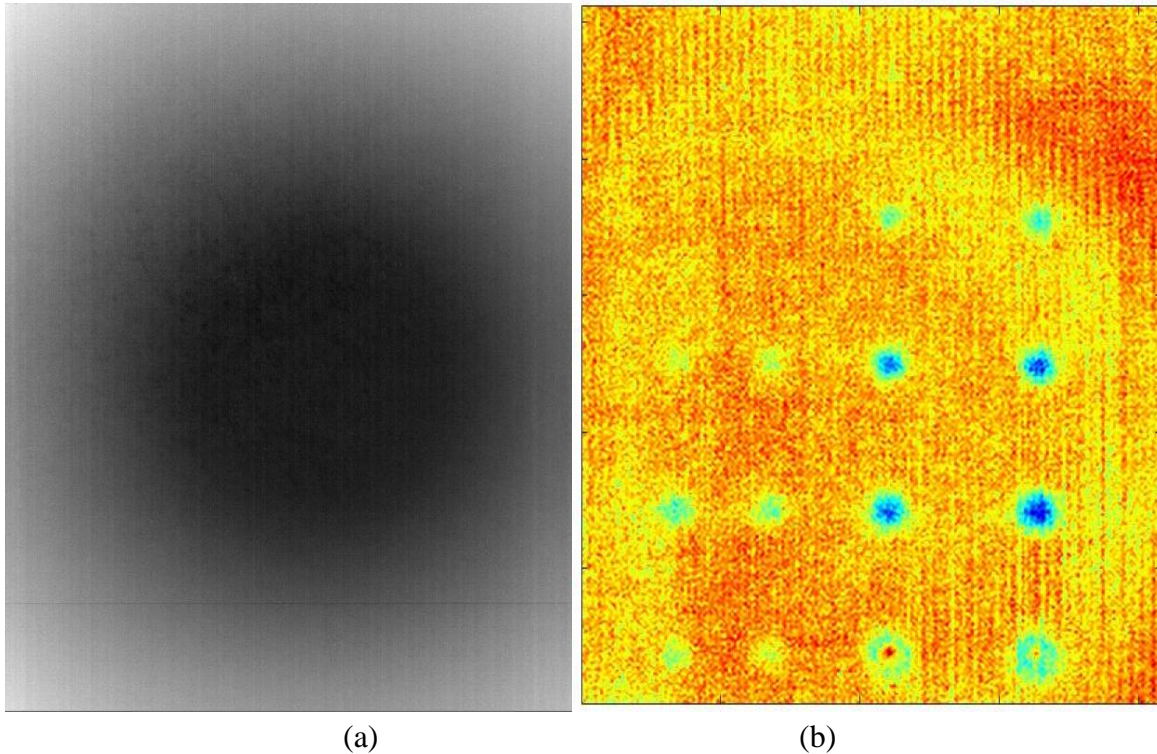
Figure 6 – Results of STDTSS detection of microscopic FBH defects in SS316 specimen. (a) Raw thermogram. (b) STDTSS image.

In the second experiment, we repeated PIT measurements with the IN718 plate. Similar to the case described above, smaller pattern of defects imprinted into the AM SS316L plate. A raw termogram is shown in Figure 7(a). Image of defects obtained with STDTSS algorithm is shown in Figure 7(b). To the best of our knowledge, detection of 200µm in IN718 with PIT is the smallest reported defect detection in literature.

(a)   (b)
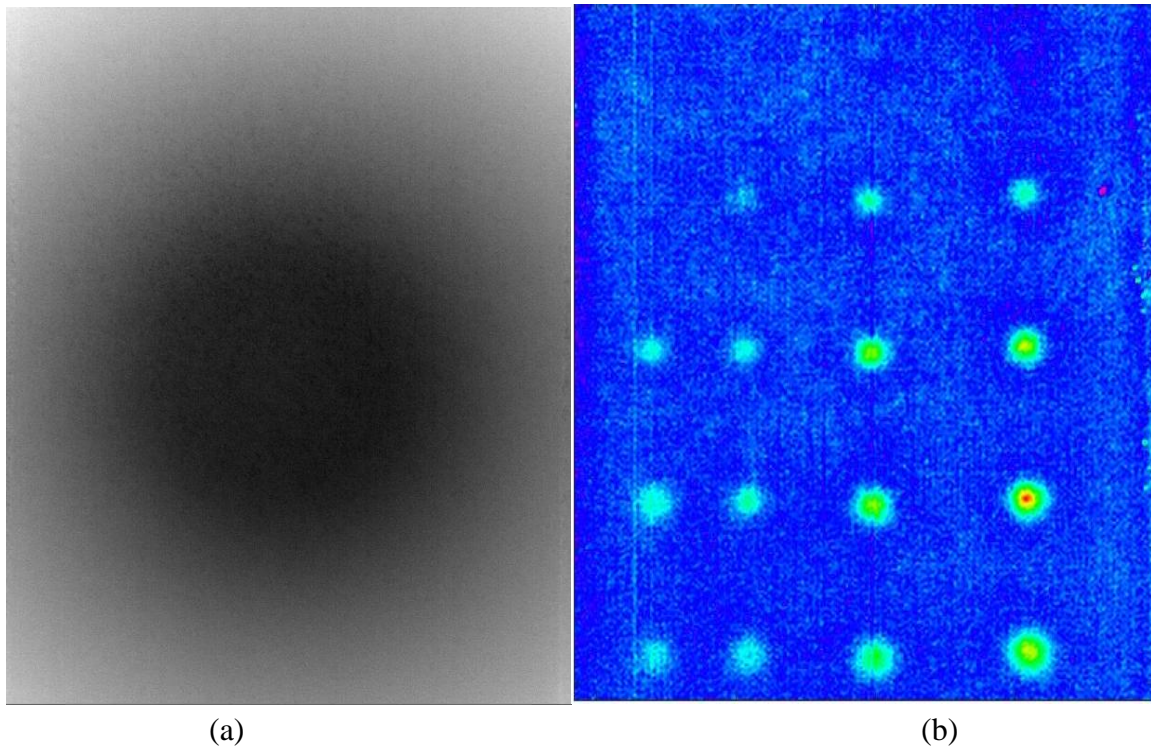
Figure 7 – Results of STDTSS detection of microscopic defects in IN718 specimen. (a) Raw thermogram. (b) STDTSS image.

4. Convolutional Neural Network (CNN) for Classification of Thermal Tomography (TT) Images

4.1. Development of Simulated Thermal Tomography Images of Metallic Plates with 2D Elliptical Defects

In this work, we develop machine learning capability to automatically extract features from thermal tomography (TT) images [14,17]. The reconstruction algorithm of TT obtains thermal effusivity $e(x,y,z)$ from time-dependent surface temperature $T(y,z,t)$ measurements. The model assumes that heat propagation is one-dimensional along the z-coordinate. For 1D heat diffusion [9]

$$\frac{\partial T}{\partial t} = \alpha \frac{\partial^2 T}{\partial x^2},$$

(5)

where x is the depth coordinate, y and z are coordinates in the transverse plane, and α is thermal diffusivity defined as

$$\alpha = k/\rho c.$$

(6)

Here, k is thermal conductivity, ρ is density, and c is specific heat. The reconstructed $e(x)$ at the location (y,z) in the plane is obtained only from the surface temperature transient T(t) measured at the location (y,z). Thermal effusivity is defined as

$$e = \sqrt{\rho c k}.$$

(7)

Following instantaneous deposition of energy on the material surface, heat diffuses into the material bulk. One can obtain the relationship between thermal wavefront depth inside the material x and time t after heat deposition as

$$x = \sqrt{\pi \alpha t}.$$

(8)

Using the analytic solution of Equation (1) for semi-infinite slabs, one can obtain the apparent effusivity as function time $e(t)$, which with the help of Equation (4) can be transformed to be function of depth $e(x)$, given as [9]

$$e(x) = x \frac{2Q}{\pi\sqrt{\alpha}} \frac{d}{dt}\left(\frac{1}{T(t)}\right)\Bigg|_{t=x^2/\pi\alpha},$$

(9)

where Q is the instantaneously deposited surface thermal energy density. Equation (9) shows that spatial reconstruction of effusivity $e(x)$ is given as a product of depth function z and time derivative of the inverse of surface temperature $T(t)$ evaluated at time t, which corresponding to depth x according to Equation (9). To calculate $e(x)$ at a particular value of x, we first calculate the corresponding time $t = x^2/\pi\alpha$, and then take the time derivative of the inverse of $T(t)$ at this time t.

Information about material internal structure is contained in recorded surface temperature transients $T(y,z,t)$ because thermal resistance of internal structures affects local surface temperature

16

decay rate. Reconstructed effusivity $e(x,y,z)$ transforms this information into spatial domain. For example, pores have lower thermal diffusivity compared to the rest of the solid material. This results in slower surface temperature decay in regions above the defects, and appearance of local temperature "hot spots." Reconstruction will show regions of lower effusivity, which can be interpreted as material defects. In this work, we display reconstructed effusivity as pseudocolor images of $e(x,y)$. Information obtained from thermography measurements is relative, but can be converted to absolute scale through calibration.

In this work, we model defects in AM steel as elliptical air voids in 2D [14,17]. We choose to use an elliptical model for the defect because thermal imaging based on heat diffusion smooths out rough edges present in the defect. This smoothing effect means that an arbitrarily shaped defect can be potentially described with an equivalent ellipse. The diagram depicting elliptical void labeling is given in Figure 8. The x-axis is along the depth of the plate, and the y-axis is along the face of the plate. The ellipse is characterized by semi-major and semi-minor axes r_x and r_y, and angular orientation θ measured from the y-axis.
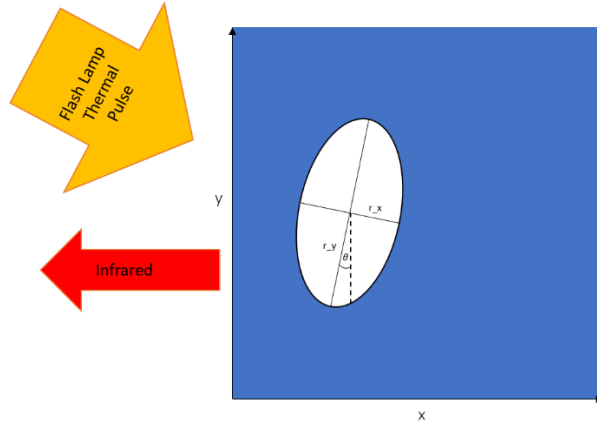
Figure 8 – Labelling of simulated defects. Depth of the plate is along the *x*-axis, and *y*-axis is along the face of the plate. The semi-major and semi-minor axes of the elliptical air void are r_x and r_y. The ellipse is rotated by an angle θ measured relative to the *y*-axis.

TT system performance for SS316 plates with elliptical defects was simulated with 2D heat transfer using MATLAB PDE Toolbox. Three examples of effusivity reconstruction of SS316 plates with dimensions 5mm x 5mm containing defects ($r_x = 160\mu m$, $r_y = 310\mu m$ and $\theta = 0°$), ($r_x =260\mu m$, $r_y = 310\mu m$, and $\theta = 45°$), and ($r_x = 60\mu m$, $r_y = 210\mu m$ and $\theta = -15°$) are shown below in Figures 9(a), 9(b) and 9(c), respectively. Reconstructions were performed for assumed imaging frame rate of 540Hz and 340 pixels spatial sampling of 5mm-long surface line.
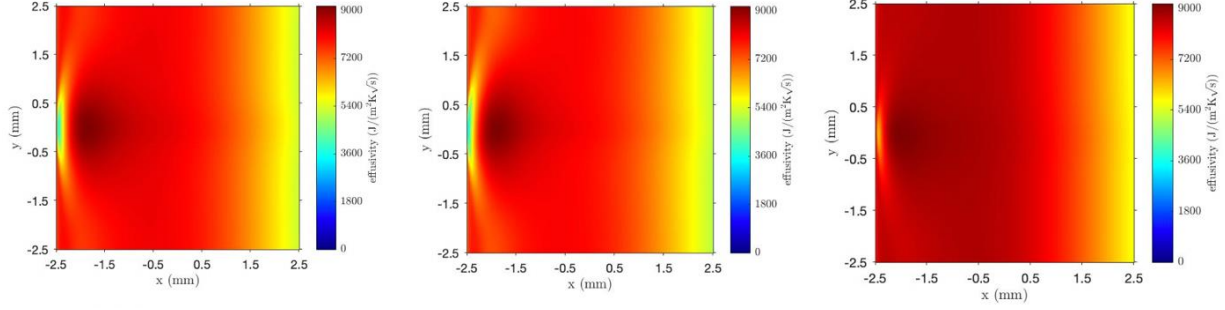
Figure 9 – Simulated effusitvity reconstruction of SS316 plate containing elliptical defects. (a) r_x = 160μm, r_y = 310μm, θ = 0°. (b) r_x = 260μm, r_y = 310μm, θ = 45° (c) r_x = 60μm, r_y = 210μm, θ = -15°

4.2. Development of Convolutional Neural Network (CNN)

We developed a deep learning convolutional neural network (CNN) for classification of defects in effusivity reconstruction images [14,17,27]. The CNN takes effusivity reconstruction images as inputs, and returns characteristic dimensions r_x, r_y, and θ of the elliptical defects. The flow chart of CNN algorithm is shown in Figure 10. To construct the CNN, we used AutoKeras's image classification class. There are four layers to the CNN: The input node is ImageInput, specific to images as represented by a Python numpy array. The training and test images in the input layer of CNN are of the same size. Following the input node, the CNN uses two AutoKeras blocks— ConvBlock and DenseBlock. AutoKeras is unique in that arguments are tuned automatically, and therefore left initially unspecified. ConvBlock includes convolutional and pooling layers required for the CNN, and DenseBlock encompasses the fully connected network following the convolutional layers. In the CNN process, convolution layers are followed by pooling layers, until a flattening layer compresses the data into a one-dimensional array. Convolution layers consists of identical neurons that are connected to local neurons in previous layer. As the neuron, or filter, operates on parts of the input image, its pixel values are multiplied by the filter values. This convolution operation creates a "feature map" from the original image. This allows features of the image to be isolated and identified. More convolution layers allow the CNN to detect lower-level features within the image, which is why convolution layers are usually stacked. Pooling layers— in this case max pooling layers—are also utilized between convolution layers to keep feature maps generalized. Max pooling takes the maximum value from each segment of the feature map produced by a given convolutional layer. Thus, pooling is necessary to ensure that the CNN is sensitive to small translations in the input. After flattening, this array is passed through a traditional fully connected (dense) layer to make the final prediction.
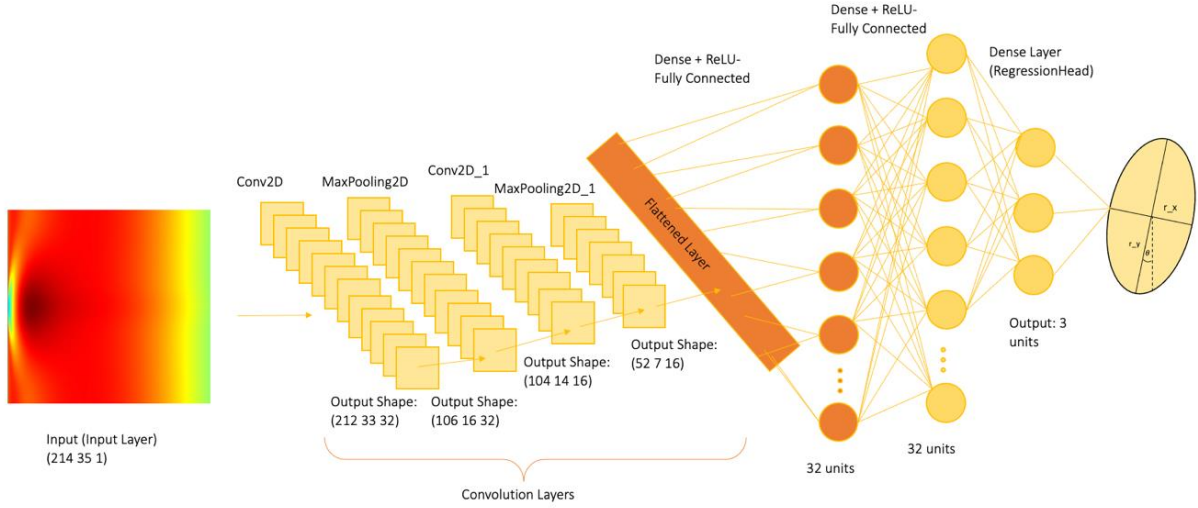
Figure 10 – Flowchart of CNN algorithm

A CNN has some advantages over a fully connected network, especially in image analysis and classification. The CNN's feature map makes it particularly adept at detecting the subtle features important aspects of images, crucial for image classification. Additionally, CNN uses copies of the same neuron to process data, which saves both time and memory. As a result, training and prediction computer running time of the CNN is less than 150 seconds on average.

4.3. CNN Classification of Elliptical Defects in Simulated TT Images

The training set for CNN consisted of 100 simulated thermal effusivity images for plates with elliptical defects with different sizes and angular orientations. The defects range in size from $20 \, x \, 20 \, \mu$m to $310 \, x \, 310 \, \mu$m with angular orientations in the range from -45° to 45°. The test set consisted of 15 different images, which were not part of the training set. Performance of CNN in classification of defects in 10 TT images in the test set is illustrated in Figure 11. Characteristic dimensions of defects are displayed as points in r_x-r_y-θ feature hyperspace diagram. Actual defects are indicated with circles, and predictions with CNN are indicated with squares. Qualitatively, the error in CNN predictions is quite small.

19
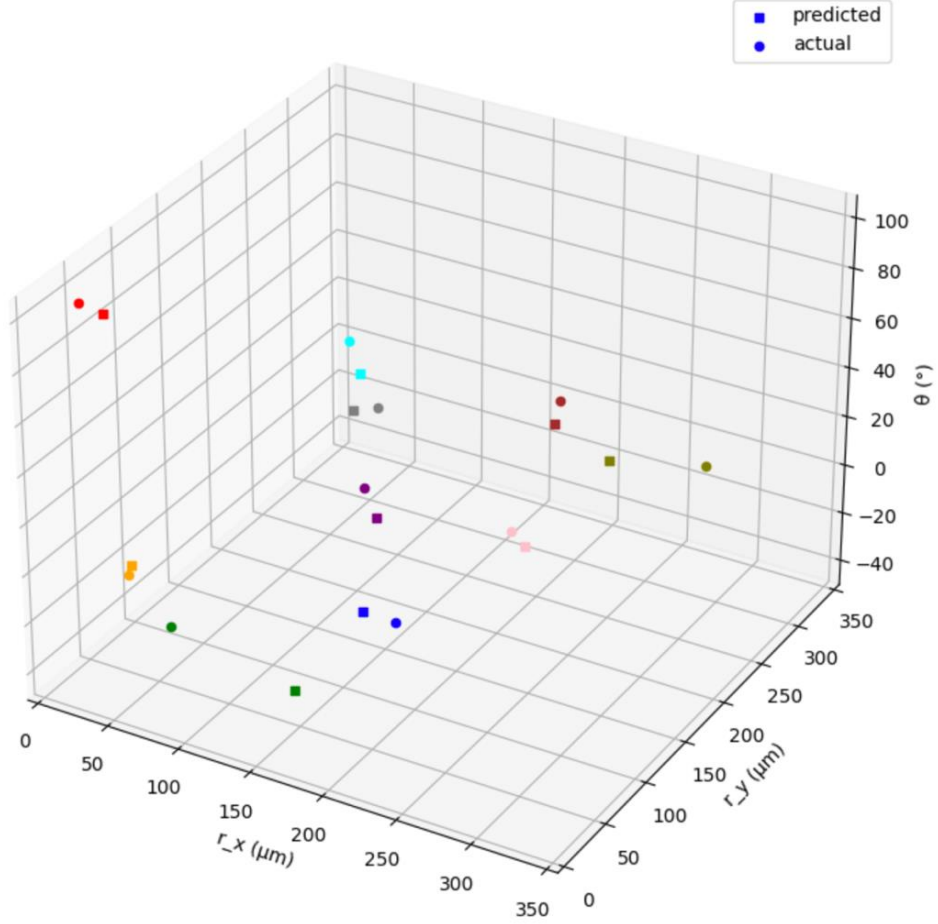
Figure 11 – Actual and predicted (classified by CNN in TT images) elliptical defects indicated by points in r_x-r_y-θ feature hyperspace diagram. Predictions are marked with squares and actual defects are marked as circles

Figure 12 illustrates CNN performance in classification of elliptical defects in simulated TT images by displaying on the same set of axis ellipses corresponding to actual and predicted set of r_x, r_y, and θ values. The actual defects in test TT images are drawn with green color. Ellipses predicted with CNN are shown in blue. Parameters of the four actual elliptical defects shown in Figures 6(a) through 6(d) are (r_x = 360μm, r_y = 60μm, θ = 0°), (r_x = 60μm, r_y = 310μm, θ = 0°), (r_x = 110μm, r_y = 260μm, θ = 30°), (r_x = 310μm, r_y = 160μm, θ = -40°). Qualitatively, predictions obtained with CNN have a relatively small error.

(a)

(b)

(c)

(d)
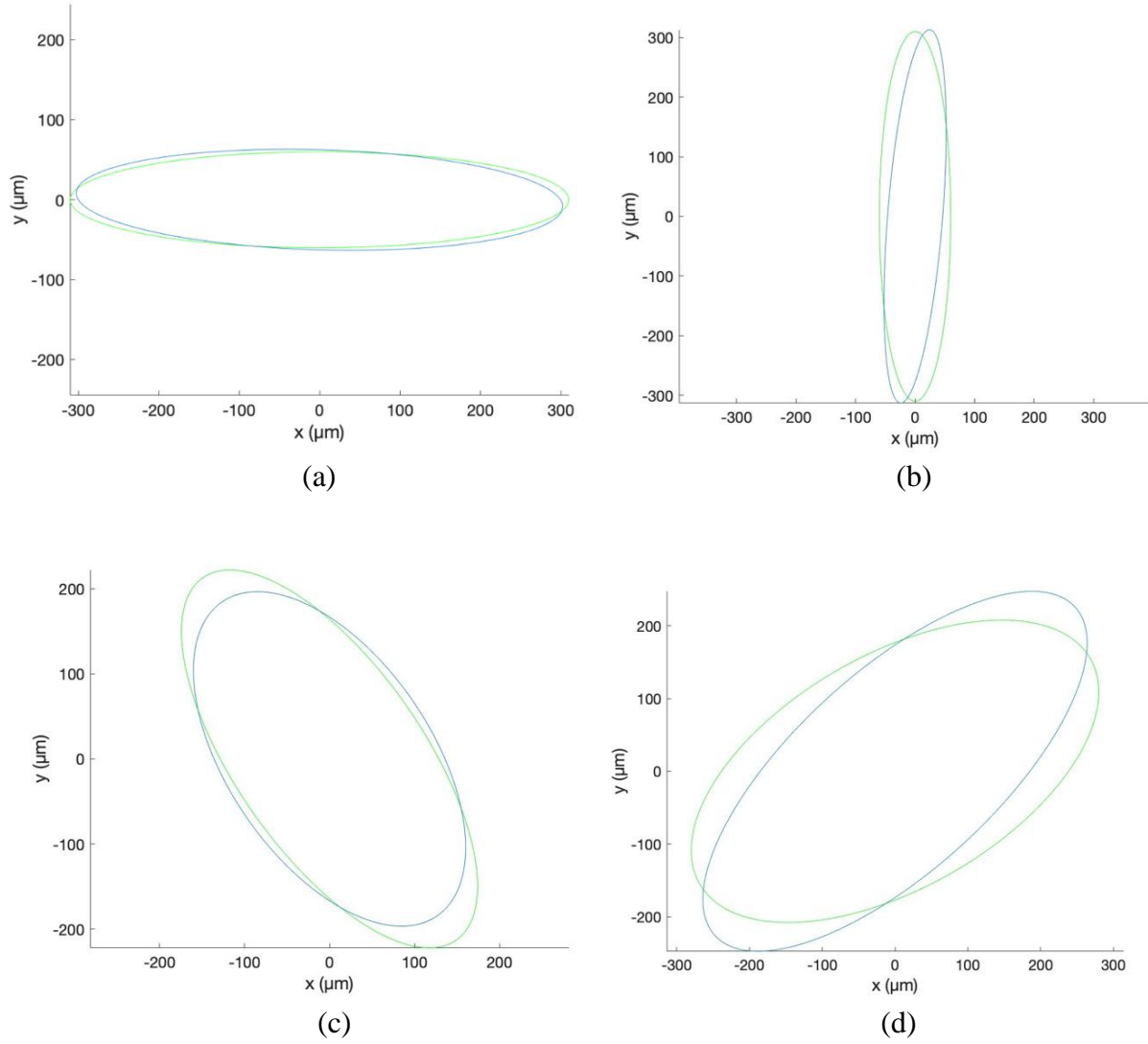
Figure 12 – Actual elliptical defects in test TT images (green) and ellipses predicted by CNN (blue). Parameters of actual defects are (a) $r_x = 360\mu m$, $r_y = 60\mu m$, $\theta = 0°$; (b) $r_x = 60\mu m$, $r_y = 310\mu m$, $\theta = 0°$ (c) $r_x = 110\mu m$, $r_y = 260\mu m$, $\theta = 30°$; (d) $r_x = 310\mu m$, $r_y = 160\mu m$, $\theta = -40°$

4.4. CNN Classification of Defects from SEM Images of LPBF SS316 in Simulated TT Images

We investigate if CNN trained on TT images with elliptical defects is capable of classifying irregular shape defects. For this study, we use SEM (scanning electron microscopy) images of actual defects in LPBF SS316 specimens. One example of such defect is shown in Figure 13(a). To characterize this defect we extract the shape from the SEM image and fit an ellipse with an equivalent surface area. For the defect in Figure 13(a), we estimate that $r_x = 43\mu m$, $r_y = 75\mu m$, and $\theta = 37°$. The air voids with the shape extracted from the SEM image are shown in Figures 13(b) to

21

13(d). Angular orientations are $\theta = 37^\circ$, $\theta = 53^\circ$ and $\theta = 8^\circ$, respectively. TT images were developed by creating plate structures with embedded air voids with the shapes of the defects shown in Figures 13(b) to 13(d), performing heat transfer calculations with MATLAB, and calculating thermal effusivity reconstructions. CNN predictions are shown in Figures 13(b) to 13(d) with blue ellipses.

(a)

(b)

(c)

(d)

Figure 13 – (a) SEM image of defect with equivalent ellipse dimensions $r_x = 43\mu m$, $r_y = 75\mu m$. (b) – (d) Air voids and CNN predictions with CNN (blue). Angular orientations: (b) $\theta = 37^\circ$; (c) $\theta = 43^\circ$; (d) $\theta = 8^\circ$

Another defect in LPBF SS316 imaged with SEM is shown in Figure 14(a). We following the same procedure of extracting the shape from SEM image, and fitting an equivalent area ellipse. The size of the equivalent ellipse for the defect in Figure 14(a) is $r_x = 10\mu m$ and $r_y = 37\mu m$, with $\theta = 19^\circ$ orientation. Figures 14(b) to 14(d) show CNN predictions (blue ellipses) for TT images with embedded rotated air void. Angular orientations of ellipses CNN associates with the defects

in Figures 14(b) to 14(d) are $\theta = 18°$, $\theta = -42°$ and $\theta = 1°$. Qualitatively, the error in CNN predictions is relatively small.
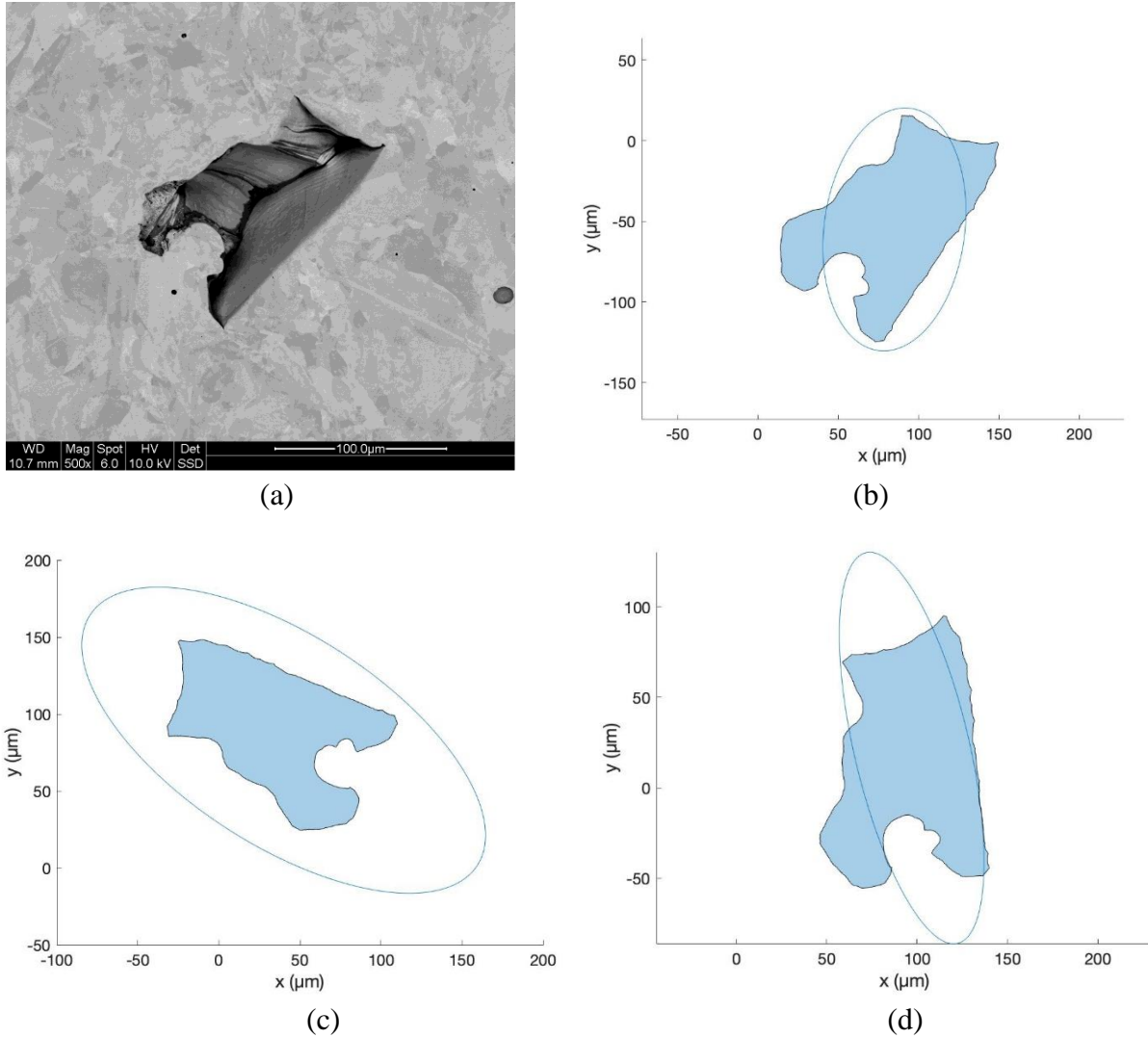

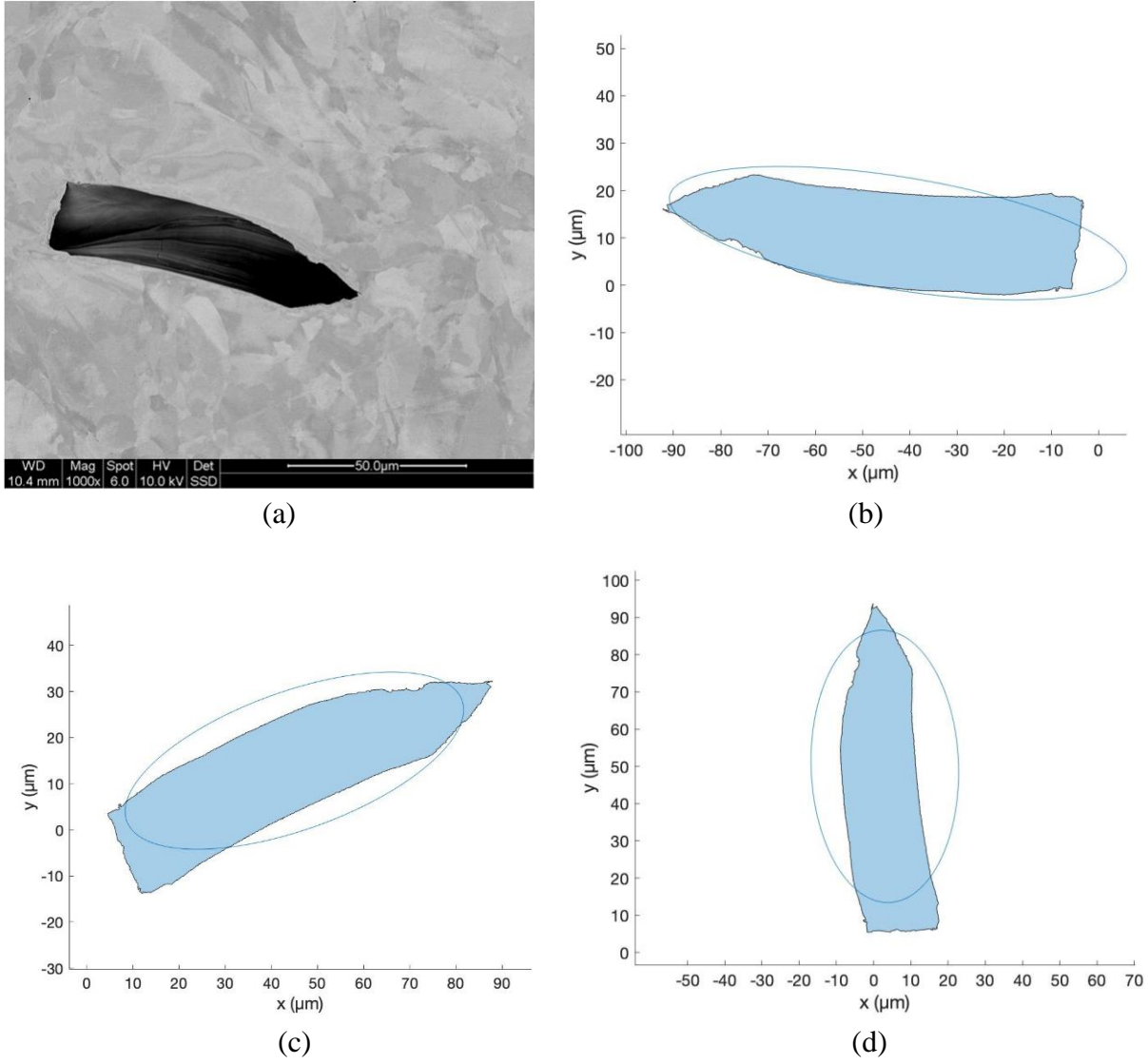(a)   (b)

(c)   (d)

Figure 14 – (a) SEM image of defect with equivalent ellipse dimensions of $r_x = 10µm$ and $r_y = 37µm$, $\theta = 19°$. (b) – (d) CNN prediction of angular orientation (blue ellipse): (b) $\theta = 18°$ (c) $\theta = -42°$ (d) $\theta = 1°$

5. Conclusions

The pulsed infrared thermography (PIT) method has advantages for NDE of actual AM structures because the method involves one-sided non-contact measurements and fast processing of large sample areas captured in one image. Following initial qualification of an AM component for deployment in a nuclear reactor, a PIT system can also be used for in-service nondestructive evaluation (NDE) applications. We have developed machine learning (ML)-based image processing methods for detection microscopic defects, and for shape and orientation classification of material defects from thermal images.

In one approach, we have investigated detection of microscopic subsurface defects in SS316 and IN718 specimens with PIT and ML-based STDTSS image processing algorithm. FBH defects with variable diameters and depths below the plate surface were created with EDM drilling. After PIT imaging, data was processed with STDTSS algorithm to obtain visualizations of the microscopic defects. To the best of our knowledge, detection of 200μm FBH with PIT is the smallest reported defect detection in NDE literature.

In future work, we will investigate detection of defects smaller than 200μm in SS316 and IN718. This is non-trivial because creating such defects requires special purpose microscopy EDM equipment, which is not widely available. To further enhance flaws detection, future work will involve optimizing the STDTSS by utilizing either sparse PCA or non-linear PCA. Further improvements in thermography hardware and ML algorithms would be needed to detect smaller and deeper-located defects, such as increasing the power of the flash lamp, and using a microscopic lens to increase the number of pixels per an image of a defect could enhance detection resolution.

In another approach, we have described development of a deep learning convolutional neural network (CNN) to classify size and orientation subsurface defects in simulated thermal tomography (TT) images. CNN is trained on a database of TT images created for a set of simulated metallic structures with elliptical subsurface voids. TT images were created with MATLAB PDE Toolbox heat transfer calculations for 2D structures. Test of CNN performance demonstrate the ability to classify radii and angular orientation of subsurface defects in TT images. In addition, we have shown that CNN trained on elliptical defects is capable of classifying irregular-shaped defects obtained from scanning electron microscopy (SEM) of stainless steel sections printed with LPBF.

In future developments, we plan extend our method to the classification of 3D defects. This can be accomplished by calculating heat transfer in 3D for a structure containing an internal defect. The CNN can be modified to take 3D arrays as an input and perform classification of 3D defect shapes. In addition, in both 2D and 3D models, we can test CNN in detecting of cracks in TT images. Good performance of CNN classification of ellipses elongated in the direction perpendicular to the plate surface gives an indication that crack detection using this computational technique is possible.

References

1. X. Lou and D. Gandy, "Advanced Manufacturing for Nuclear Energy," *JOM* 71, 2834-2836 (2019).

2. W.E. King, A.T. Anderson, R.M. Ferencz, N.E.Hodge, C. Kamath, S.A. Khairallah, and A.M. Rubenchik, "Laser powder bed fusion additive manufacturing of metals: physics, computational and materials challenges," *Appl. Phys. Rev.* 2, 041304 (2015).

3. S. A. Khairallah, A. T. Anderson, A. Rubenchik, W. E. King, "Laser Powder-Bed Fusion Additive Manufacturing: Physics of Complex Melt Flow and Formation Mechanisms of Pores, Spatter and Denudation Zones," *Acta Materialia* 108, 36-45 (2016).

4. 2.C. Hensley, K. Sisco, S. Beuchamp, A. Godfrey, H. Rezayat, T. McFalls, D. Galicki, F. List III, K. Carver, C. Stover, D.W. Gandy, S.S Babu, "Qualification Pathways for Additively Manufactured Components for Nuclear Applications," *J. Nucl. Mater*. 548, 152846, May 2021.

5. M. D. Sangid, P. Ravi, V. Prithivirajan, N. A. Miller, P. Kenesei, J.-S. Park, "ICME Approach to Determining Critical Pore Size of IN718 Produced by Selective Laser Melting," *JOM* 72, 465-474 (2019).

6. S. Tammas-Williams, P. J. Withers, I. Todd, and P.B. Prangnell, "The Influence of Porosity on Fatigue Crack Initiation in Additively Manufactured Titanium Components," *Scientific Reports* 7, 7308 (2017).

7. X. Zhang, J. Saniie, W. Cleary, A. Heifetz. (2020). "Quality Control of Additively Manufactured Metallic Structures with Machine Learning of Thermography Images," *JOM* 72(12), 4682-4694 (2020).

8. X. Zhang, J. Saniie, A. Heifetz, "Detection of Defects in Additively Manufactured Stainless Steel 316L with Compact Infrared Camera and Machine Learning Algorithms," *JOM* 72(12), 4244-4253 (2020).

9. A. Heifetz, D. Shribak, X. Zhang, J. Saniie, Z.L. Fisher, T. Liu, J.G. Sun, T. Elmer, S. Bakhtiari, W. Cleary, "Thermal Tomography 3D Imaging of Additively Manufactured Metallic Structures," *AIP Advances* 10(10), 105318 (2020).

10. X. Zhang, J. Saniie, A. Heifetz, "Neural Learning Based Blind Source Separation for Detection of Material Defects in Pulsed Thermography Images," *Proc. 2020 IEEE Intern. Conf. Electro-Information Technology (EIT)*, 112-116 (2020).

11. X. Zhang, J. Saniie, A. Heifetz, "Spatial Temporal Denoised Thermal Source Separation in Images of Compact Pulsed Thermography System for Qualification of Additively Manufactured Metals," *Proc. 2021 IEEE Intern. Conf. Electro- Information Technology (EIT)*, 209-214 (2021).

12. A. Heifetz, J.G. Sun, D. Shribak, T. Liu, T.W. Elmer, P. Kozak, S. Bakhtiari, B. Khaykovich, W. Cleary, "Pulsed Thermal Tomography Nondestructive Evaluation of Additively Manufactured Reactor Structural Materials," *Trans. Am. Nucl. Soc*. 121(1), 589-591 (2019).

13. A. Heifetz, D. Shribak, Z.L. Fisher, W. Cleary, "Detection of Defects in Additively Manufactured Metals Using Thermal Tomography," *TMS 2021 150th Annual Meeting & Exhibition Supplemental Proceedings*, 121-127 (2021).

14. V. Ankel, D. Shribak, A. Heifetz, "Defect Classification in Simulated Pulsed Thermal Tomography Images using Deep Learning Convolutional Neural Network," *Trans. Am. Nucl. Soc.* 125(1), 102-105 (2021).

15. A. Heifetz, X. Zhang, J. Saniie, D. Shribak, T. Elmer, S. Bakhtiari, B. Khaykovich, W.L. Cleary, "Second Annual Progress Report on Pulsed Thermal Tomography Nondestructive Examination of Additively Manufactured Reactor Materials," ANL-20/62 (2020).

16. A. Heifetz, X. Zhang, J. Saniie, S. Bakhtiari, "Performance Validation of Pulsed Thermal Imaging System for In-Service Applications," ANL-21/35 (2021).

17. A. Heifetz, V. Ankel, D. Shribak, W.-Y. Chen, "Performance of Pulsed Thermal Tomography Imaging with Machine Learning-Based Classification of Defects in Additively Manufactured Structures," ANL-21/40 (2021).

18. F. Garrido, A. Salazar, F. Alonso, and I. Sáez-Ocáriz, "Characterization of buried cylinders and spheres by pulsed infrared thermography*," J. Appl. Phys.* 98, 103502 (2005).

19. J. C. Ramirez-Granados, G. Paez, and M. Strojnik, "Three-dimensional reconstruction of subsurface defects using finite-difference modeling on pulsed thermography," *Appl. Opt*. 51, 154288 (2012).

20. P. Kovács, B. Lehner, G, Thummerer, G. Mayr, P. Burgholzer, and M. Huemer, "Deep learning approaches for thermographic imaging," *J. Appl. Phys.* 128, 155103 (2020).

21. D.L. Balageas, J.M. Roche, F.H. Leroy, W.M. Liu, A.M. Gorbach, "The Thermographic Signal Reconstruction Method: A Powerful Tool for the Enhancement of Transient Thermographic Images," *Biocybern. Biomed. Eng*. 35(1), 1-9 (2014)

22. G. Mayr, G. Stockner, H. Plasser, G. Hendorfer, P. Burgholzer, "Parameter Estimation from Pulsed Thermography Data using the Virtual Wave Concept," *NDT E Int.* 100, 101-107 (2018).

23. P. Burgholzer, M. Thor, J. Gruber, and G. Mayr, "Three-dimensional thermographic imaging using a virtual wave concept," *J. Appl. Phys.* 121, 105102 (2017).

24. S.C. Wu, B. Gao, Y. Yang, Y.Y. Zhu, P. Burrascano, S. Laureti, M. Ricci, Y.Z. Wang, "Halogen Optical referred Pulse-Compression Thermography for Defect Detection of CFRP," *Infrared Phys. Technol.* 102, 103006 (2019).

25. J. Ahmad, A. Akula, R. Mulaveesala and H. K. Sardana, "Barker-Coded Thermal Wave Imaging for Non-Destructive Testing and Evaluation of Steel Material," *IEEE Sens. J* 19(2), 735-742 (2019).

26. W. F. Da Silva, R. A. C. Melo, M. Grosso, G. R. Pereira and D. B. Riffel, "Active Thermography Data-Processing Algorithm for Nondestructive Testing of Materials," *IEEE Access* 8, 175054-175062 (2020).

27. Y. Bengio, Y. LeCun, G. Hinton, "Deep Learning," *Nature* **521** (7553), 436–444 (2015).

Nuclear Science and Engineering (NSE) Division
Argonne National Laboratory
9700 South Cass Avenue, Bldg. 208
Argonne, IL 60439

www.anl.gov